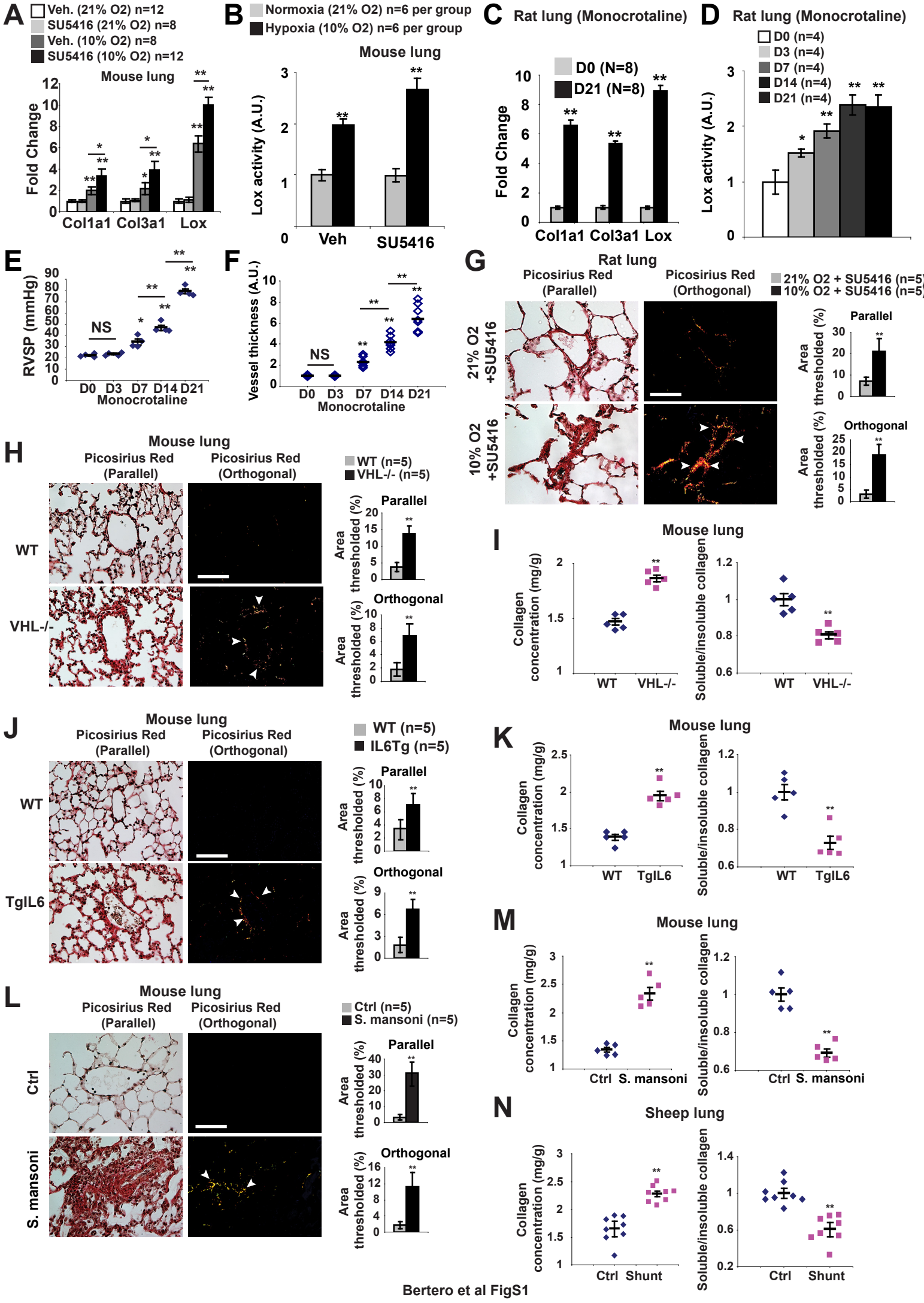

Bertero et al FigS1

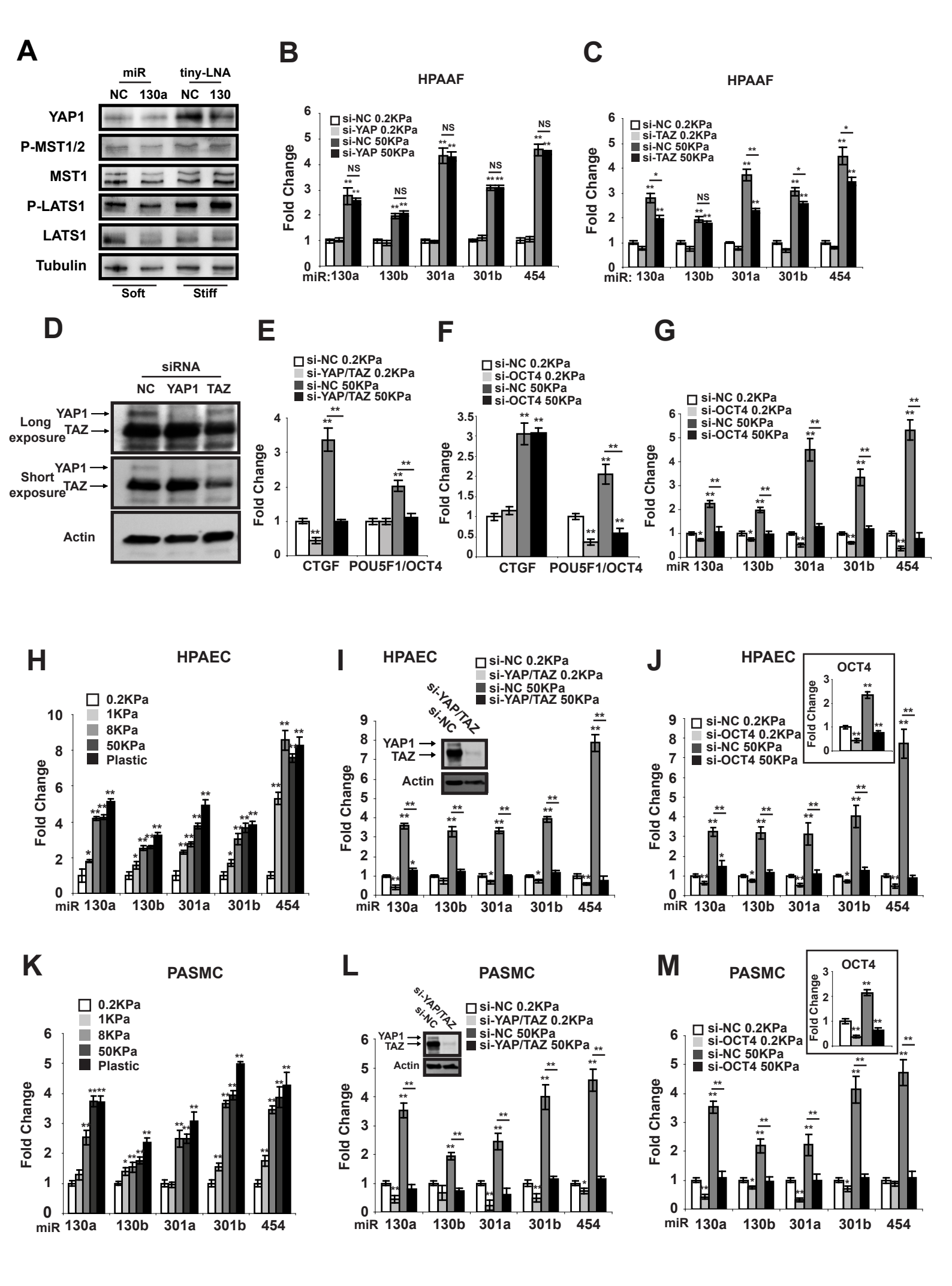

Bertero et al FigS2

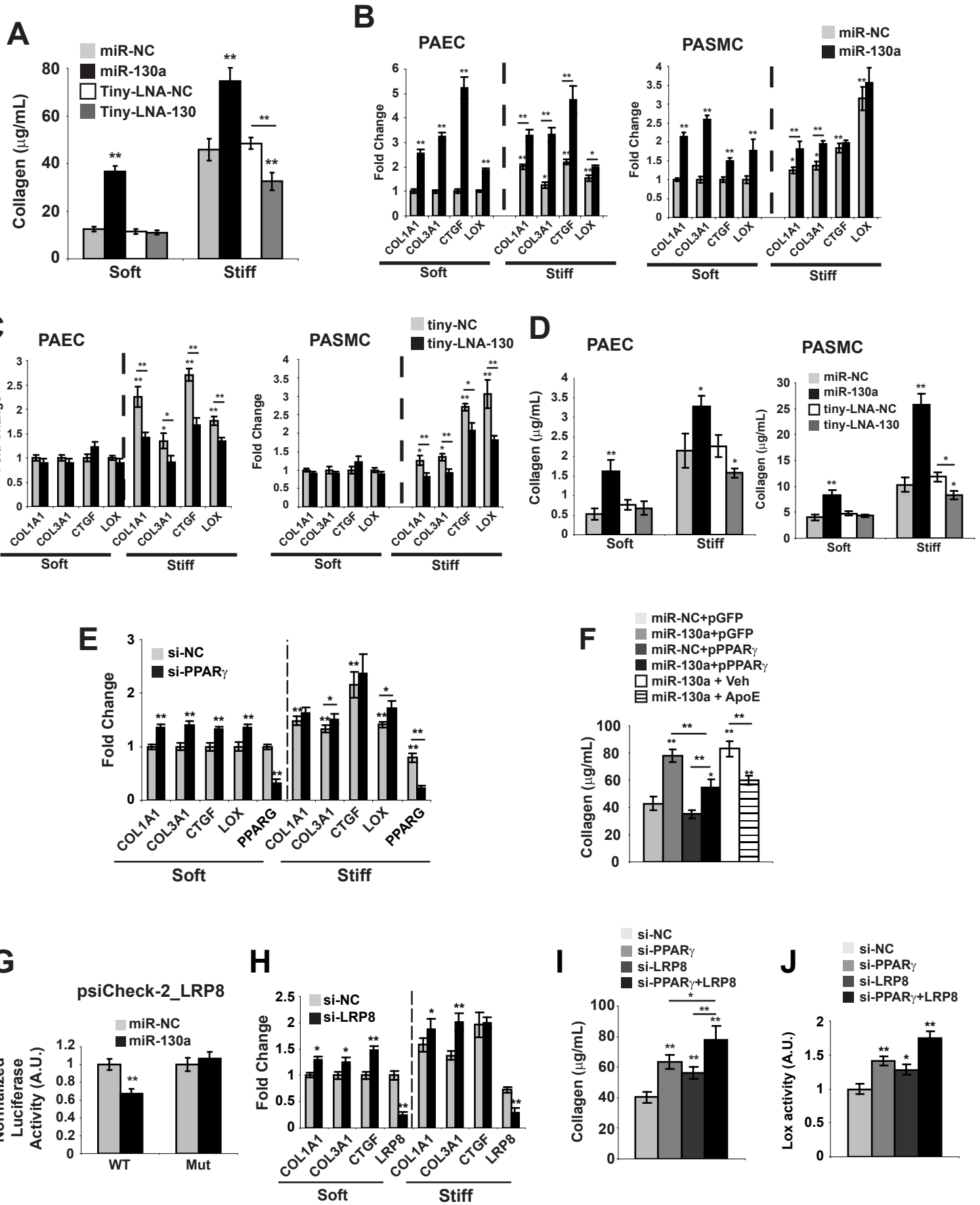

Bertero et al FigS3

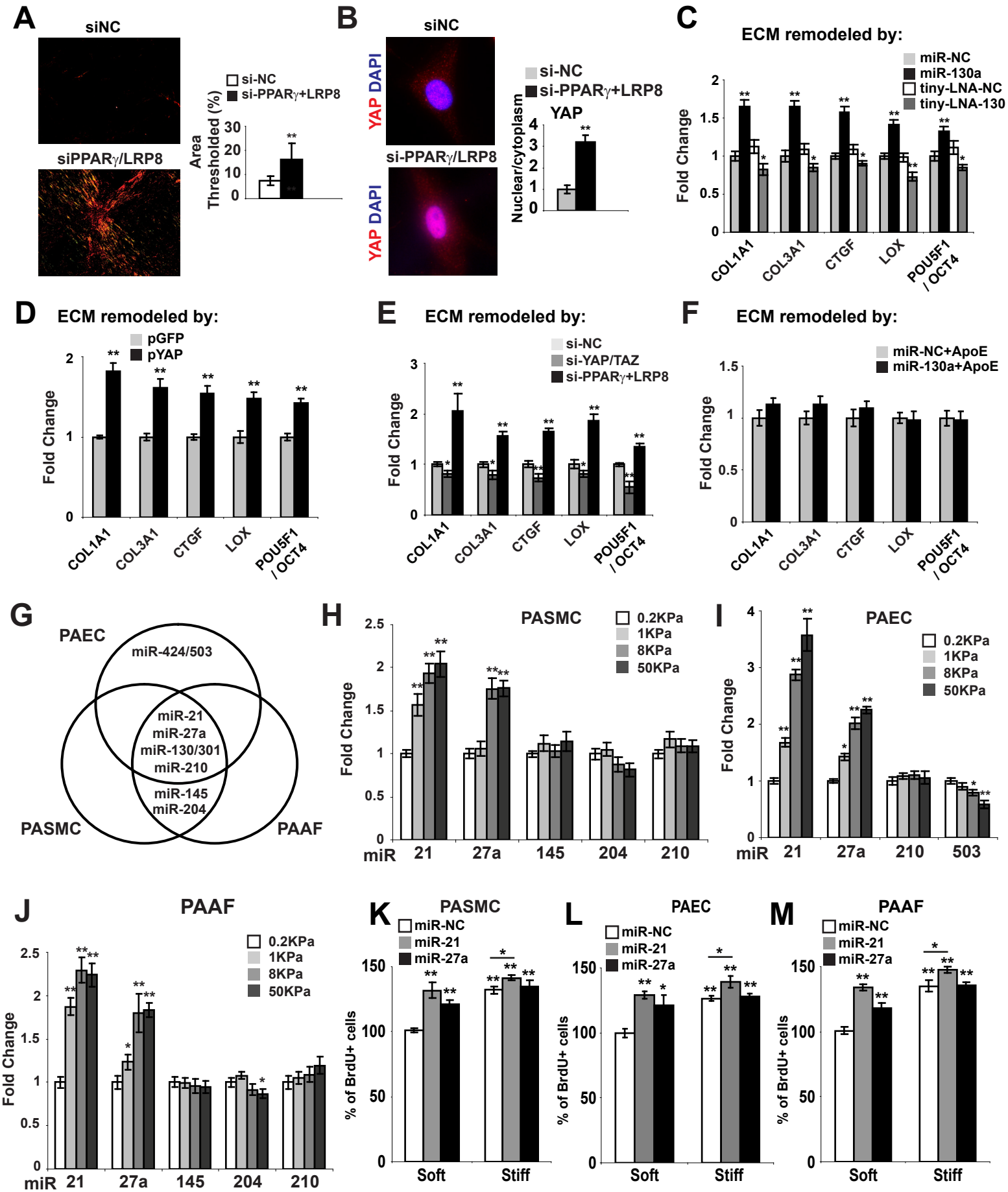

Bertero et al FigS4

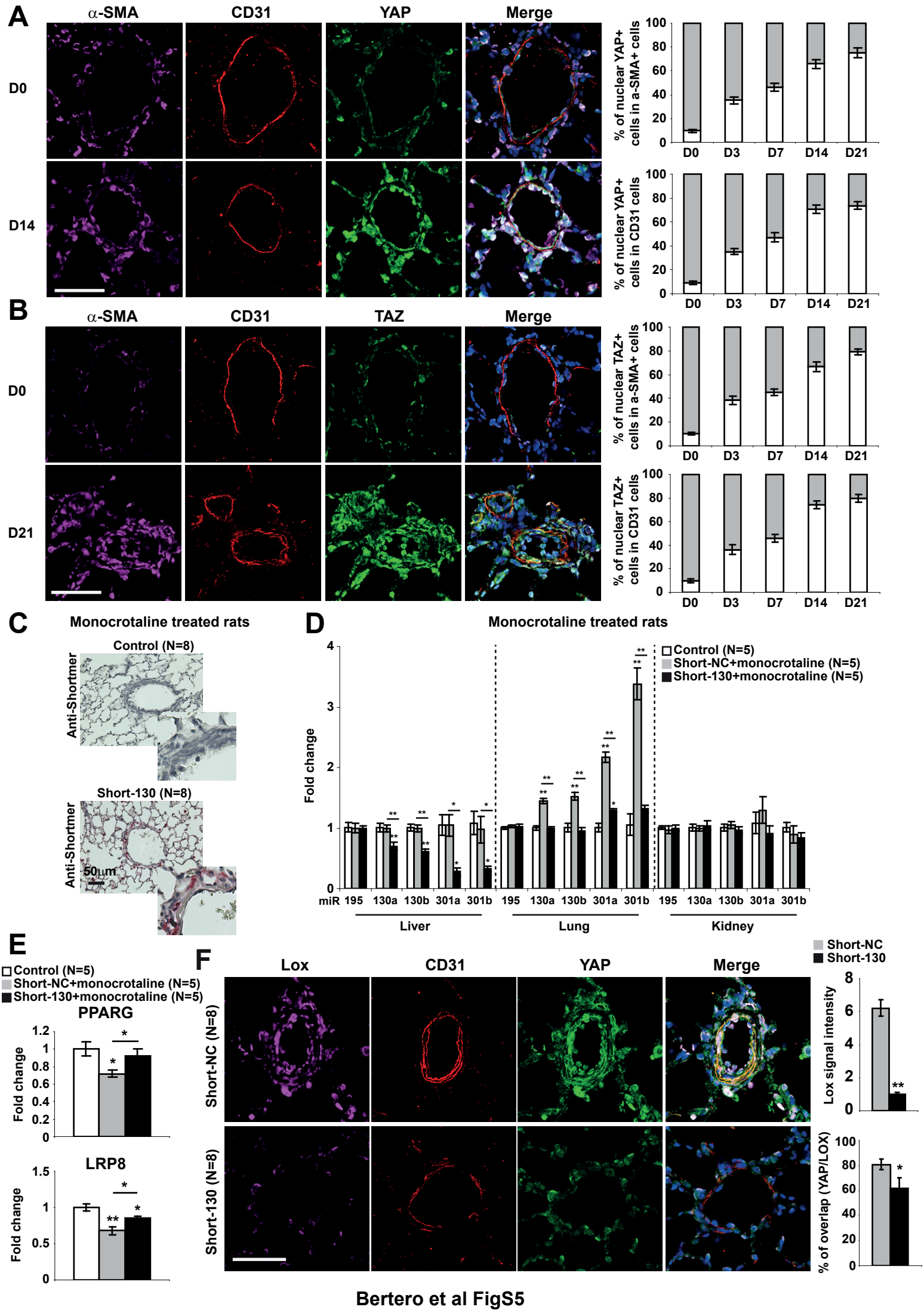

Bertero et al FigS5

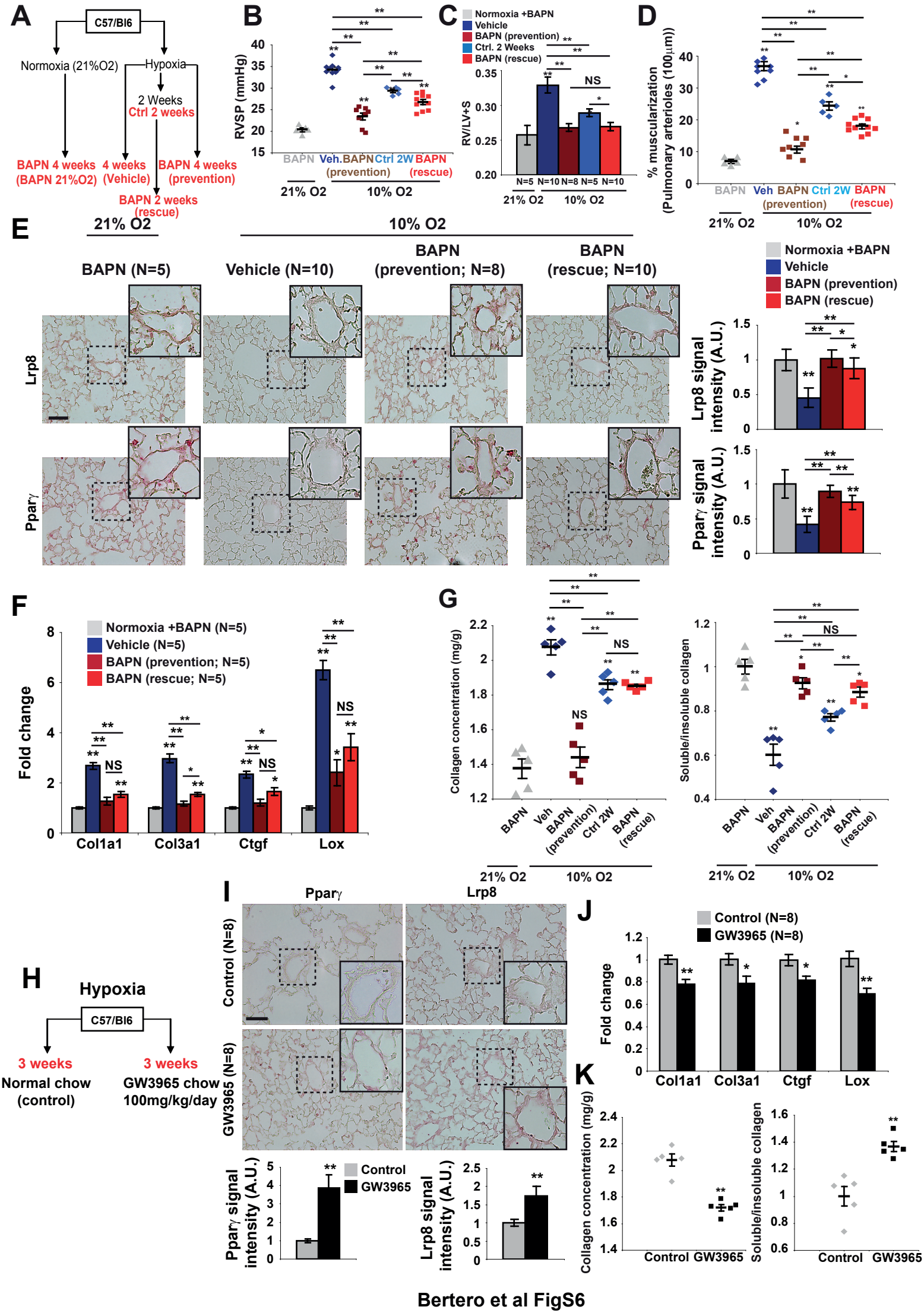

Bertero et al FigS6

Supplemental Figure Legends

Figure S1: Collagen deposition and remodeling in small pulmonary arterioles are hallmarks of PH (Related to Fig. 1). A-B) PH was induced in mice by hypoxia +/- SU5416 (10% O_2 for 3 weeks). Increased expression of collagen isoforms and the collagen crosslinking gene LOX (n=8-12/group) (**A**) as well as increased LOX activity (n=6 per group) (**B**) were observed in diseased lung. **C-F)** Monocrotaline was administered to rats (3 weeks, n=6-8/time point). As in hypoxic mice, collagen and LOX expression (n=8/group) (**C**) as well as LOX activity (n=4 per group) were increased (**D**). PH severity was measured by RVSP (**E**) and pulmonary arteriolar thickness (**F**). **G)** Picrosirius Red stain of rat lung treated with the VEGF receptor antagonist SU5416 in combination with chronic hypoxia (10% O_2 for 3 weeks) as compared with normoxia+SU5416 was imaged in parallel light to display total collagen content (top) or orthogonal light to display fibrillar collagen content (bottom) (10 vessels < 100μm per rat). Imaging revealed an increase in collagen expression and fibrillar collagen under disease conditions (n=5/group). **H)** Picrosirius Red coloration of lung tissues was imaged in knockout VHL mice (VHL-/-) (10 vessels < 100μm per mouse, n=5/group). **I)** Soluble and insoluble fractions of collagen in lung were also confirmed by Sircol assay (n=5/group). **J-M)** Such results were confirmed in other mouse models of PH (n=5/group), including interleukin-6 transgenic mice (TgIL6; **J-K**) and mice infected by S. *mansoni* (*S. mansoni*) (**L-M**). **N)** In juvenile sheep with PAH secondary to a surgically

placed pulmonary artery-aortic shunt (n=8) as compared with sham surgical controls (n=8), Sircol assays revealed an increase in collagen expression and fibrillar collagen under disease conditions. Data are expressed as mean ± SEM (*P<0.05; ** P<0.01). See also **Fig. 1**.

Figure S2: Tissue mechanics regulate miR-130/301 expression in a YAP-dependent and TAZ-dependent manner (Related to Fig. 2). Pulmonary artery smooth muscle cells (PASMCs), pulmonary artery endothelial cells (PAECs), and pulmonary artery adventitial fibroblasts (PAAF) were cultured on collagen-coated hydrogels of varying stiffness. **A)** Immunoblots demonstrated the levels of active (phosphorylated) P-MST1/2 (quantified by pT183/T180), MST1, active (phosphorylated) LATS1 (judged by pT1079), LATS1, YAP, and tubulin loading control in PAAFs transfected with miR-NC, miR-130a, tiny-LNA-NC or tiny-LNA-130 and cultured in soft and stiff matrix. Stiff matrix increased the expression of YAP1, but neither total nor phosphorylated forms of LATS1 or MST1/2 kinases were concomitantly modulated by stiffness. Additionally, neither forced miR-130a expression nor inhibition of miR-130/301 modulated the LATS1 or MST1/2 isoforms. **B-D)** In human PAAFs, siRNA knockdown of YAP (**B**) or TAZ (**C**) alone did not reverse the ECM stiffness-induced expression of miR-130/301 family members. **D)** As demonstrated by immunoblot, siRNA knockdown of YAP and TAZ was effective in human PAAFs. **E-G)** Transcripts of CTGF and POU5F1/OCT4, both of which are direct gene targets of YAP/TAZ, were quantified in PAAFs transfected with siRNAs to YAP/TAZ (**E**) or POU5F1/OCT4 (**F**). Expression of miR-130/301 was induced by stiffness and was decreased by POU5F1/OCT4 knockdown (**G**). **H-M**) In PAECs and

PASMCs, expression of miR-130/301 was induced by stiffness **(H,K)**, and was dependent on YAP/TAZ (**I,L**) and POU5F1/OCT4 (**J,M**). In all panels, mean expression in control groups (si-NC on soft matrix) was assigned a fold change of 1, to which relevant samples were compared. Data are expressed as mean ± SD (*P<0.05; ** P<0.01).

Figure S3: The miR-130/301 family modulates ECM properties through the PPARγ-APOE-LRP8 regulatory axis in pulmonary arterial cells (Related to Fig. 2). A) In PAAFs, the collagen content of conditioned media was increased both by stiffness and by miR-130a, and reversed by inhibition of miR-130/301. **B)** Collagen, CTGF, and LOX were up-regulated by miR-130a overexpression in PAECs (left graph) and PASMCs (right graph). **C)** Stiffness-mediated up-regulation of collagen, CTGF, and LOX was reversed by inhibition of the miR-130/301 family (tiny-LNA-130) in PAECs (left graph) and PASMCs (right graph). **D)** In either PAECs (left graph) or PASMCs (right graph), the collagen content of conditioned media was increased both by stiffness and by miR-130a, and reversed by inhibition of miR-130/301. **E)** In PAAFs**,** siRNA knockdown of PPARγ increased collagen and LOX expression in soft matrix. **F)** In PAAFs, the collagen-content of conditioned media was increased by miR-130a and reversed by constitutive PPARγ or ApoE. **G)** Luciferase reporter assays of wild type (WT) and mutated (MUT) 3'UTR sequence of LRP8 were performed in the presence of miR-NC or miR-130a. **H)** In PAAFs**,** siRNA knockdown of LRP8 increased collagen and LOX expression in soft matrix. **I-J)** Both the collagen-content of conditioned media (**I**) and intracellular Lox activity (**J**) of PAAFs were increased by either si-PPARγ or si-LRP8 but

increased to a larger extent by siPPARγ+siLRP8 together. In all panels, mean expression in control groups was assigned a fold change of 1, to which relevant samples were compared. Data are expressed as mean ± SD (*P<0.05; ** P<0.01).

Figure S4: miR-130/301-dependent ECM modification activates a self-sustaining feedback loop (Related to Fig. 3). A-B) ECM staining by Picrosirius Red revealed that siRNA knockdown of PPARγ and LRP8 increased fibrillar collagen (**A)**. In that context, immunofluorescenct imaging for YAP (red) and nuclei (DAPI, blue) was performed on naïve PAAFs plated on ECM remodeled by the indicated conditions. Nuclear stain relative to cytosolic stain of YAP was quantified (**B**). **C-F)** RT-qPCR analysis of naïve cells (non-transfected PAAFs) plated on ECM previously remodeled by the indicated conditions revealed that either ECM remodeled by miR-130a overexpression (**C**), ECM remodeled by YAP overexpression (pYAP; **D**), or ECM remodeled by knockdown of PPARγ+LRP8 together (**E**) up-regulated collagen, LOX, CTGF, and POU5F1/OCT4. Conversely, ECM remodeled by inhibition of miR-130/301 (tiny-LNA-130) (**C**) or ECM remodeled by knockdown of YAP/TAZ (**E**) down-regulated collagen, LOX, CTGF, and POU5F1/OCT4. **F)** Finally, consistent with preventing the induction of miR-130/301 members in naïve cells cultured on matrix remodeled by miR-130a, addition of ApoE to remodeled ECM (miR-130a+ApoE cells) led to negligible alterations in transcript expression of collagen, LOX, CTGF, and POU5F1/OCT4. **G)** Venn diagram representing the cellular localization of specific miRNAs known to be involved in PH. **H-J)** Expression of PH-related miRNAs was quantified in human PASMCs (**H**), PAECs (**I**) and PAAFs (**J**) cultured in hydrogel of varying stiffness. **K-M)** Overexpression of miR-21 and miR-27a

increased cell proliferation (BrdU staining) in PASMCs, PAECs, and PAAFs under soft and stiff conditions. In all panels, mean expression in control groups was assigned a fold change of 1, to which relevant samples were compared. Data are expressed as mean ± SD (*P<0.05; ** P<0.01).

Figure S5: Short-130 inhibits the increased expression of miR-130/301 family members in lung tissue of monocrotaline-exposed rats (Related to Fig. 4,6). **A-B)** Monocrotaline (60 mg/kg) was administered to male Sprague-Dawley rats to induce PH and followed over three weeks (n=6-8/time point). Spatio-temporal expression of YAP (**A**) and TAZ (**B**) in both intimal (CD31-positive) and medial (α-SMA-positive) layers were analyzed by immunofluorescence microscopy. **C-E)** Male Sprague-Dawley rats (N=5/group) were injected with vehicle control or 60 mg/kg monocrotaline at time 0 accompanied by 5 intraperitoneal injections (every 3 days) of control or miR-130/301 shortmer oligonucleotides (20mg/kg/dose). Three days after the last injection, shortmer delivery and miRNA expression in whole lung tissue were assessed by immunochemistry (**C**) and by RT-qPCR (**D**), respectively. **E)** RT-qPCR confirmed that mRNA levels of PPARγ and LRP8, two direct targets of miR-130/301, were decreased in diseased lung, but expression was partially rescued by Short-130. **F)** Short-130-dependent alterations of LOX expression and its correlation with YAP expression in both CD31-positive and CD31-negative vessel layers were demonstrated by immunofluorescence microscopy. Data are expressed as mean ± SEM (*P<0.05; ** P<0.01).

Figure S6: Pharmacological inhibition of LOX activity with BAPN or pharmacological activation of APOE with LXR agonist GW3965 ameliorates PH (Related to Fig. 7). A) Schema for preventing (prevention) or reducing existing hypoxic PH (rescue) with BAPN. **B-D)** BAPN both prevented and reversed PH severity as quantified by RVSP **(B),** extent of right ventricular hypertrophy (Fulton index, RV/LV+S) (**C**), and extent of arteriolar muscularization (**D**). **E)** *In situ* staining of mouse lung demonstrated that BAPN either prevented or rescued hypoxia mediated decreases of Lrp8 and Pparγ. **F)** By RT-qPCR, Ctgf, collagen isoforms, and Lox were increased in diseased lung (Vehicle), but BAPN blunted these alterations. **G)** By Sircol assay (n=5/group), whole lung collagen content (left graph) and remodeled collagen content (decreased Soluble/Insoluble collagen ratio, right graph) were decreased by BAPN prevention and rescue treatment. **H)** Schema for preventing hypoxic PH with GW3965. **I)** *In situ* staining of mouse lung demonstrated that GW3965 prevented hypoxia mediated decreases of Lrp8 and Pparγ. **J)** By RT-qPCR, Ctgf, collagen isoforms, and Lox were increased in diseased lung (Control), but Gw3965 blunted these alterations. **K)** By Sircol assay (n=5/group), whole lung collagen content (left graph) and remodeled collagen content (decreased Soluble/Insoluble collagen ratio, right graph) were decreased by GW3965 treatment. Data are expressed as mean ± SEM (*P<0.05; ** P<0.01).

Supplemental Tables

TABLE S3: Genes in the fibrosis network (Related to Fig. 2). Genes were annotated by architectural cluster.

Cluster 1 (Green)	AQP3, AREG, ARF4, ATP1A1, ATP2A2, BAG4, BCL2, BCR, BLK, CAV1, CAV2, CCL11, CCR2, CD300LF, CDCA5, CEBPB, CEP135, CREB1, CSF2RB, CXCL12, CXCR4, DMBT1, DNAJA1, EGF, EGFR, ELK1, FOXM1, FYN, GAB1, GAB2, ICAM1, IL10, KSR2, LAIR1, LIFR, LILRB4, MAPK1, MAPK3, MEF2C, MUC1, NTRK1, P53AIP1, PDGFRA, PDGFRB, PPARA, PRLR, PTPN1, PTPN11, PTPN2, PTPN5, PTPN6, RPS6KA1, RPS6KA2, RPS6KA3, RPS6KA4, RPS6KA5, SDC4, SEMA7A, SH2B1, SIRPA, SPN, STAT1, STAT3, THRB, TRADD, TTK, ZAP70
Cluster 2 (Red)	ABTB1, ACVR1, APC, AXIN1, AXIN2, BMP7, COL5A3, CTNNB1, CXXC5, CXorf9, CYP11A1, DAB2, EIF2AK4, ENG, FBXL11, FBXL12, FOXO3, JUNB, LRP5, LRP6, MTMR10, MYBL1, MYC, MYO3A, NFE2L2, NFYA, NFYB, NFYC, PPARG, PPP6C, PSMD11, PTPN14, RAB25, RFX1, RHEBL1, RNF111, SFRP1, SKIL, SMAD1, SMAD2, SMAD3, SMAD4, SMAD5, SMAD6, SMAD7, SMAD9, SMARCA4, STRAP, TGFB2, TGFB3, TGFBR1, TGFBR2, TGIF1, TRIM28, TSSK1B, VASN, WNT1, WNT2, XPO1, ZEB2, ZNF8
Cluster 3 (Orange)	ANGPTL3, APP, CALR, CCL2, CCL3, CD36, CD44, CD46, CD47, CD93, CHAD, CIB1, COL13A1, COL18A1, COL1A1, COL1A2, COL3A1, COL4A1, COL4A2, COL4A3, COL4A4, COL4A5, COL4A6, COL7A1, CTGF, CXCL6, CYR61, DCN, DPT, ELN, FCER2, FIGF, HABP2, HSPG2, IGF1, IGFBP3, IL1B, ILK, ITGA2, ITGA2B, ITGA3, ITGA4, ITGA5, ITGA6, ITGA9, ITGAV, ITGB1, ITGB3, ITGB5, ITGB6, ITGB8, JAM2, KLK3, KLK6, LOX, LTBP1, MMP1, MMP13, MMP14, MMP2, MMP3, MMP7, MMP8, MMP9, NID2, NOV, PAK1, PDGFA, PDGFB, PRELP, PRKG1, SAA1, SAA2, SERPINA1, SLC3A2, SNAI1, SPARC, SPP1, TFPI, TGFB1, TGM2, THBS1, THBS2, TIMP1, TIMP2, TIMP3, TIMP4, VEGFA
Cluster 4 (Dark Blue)	ACE, AKT1, ARHGAP1, BNIPL, CAMK4, CDC42, CDGAP, DEF6, DNAJA3, EDN1, EGR1, EIF4B, EIF4E, EIF4EBP1, ERF, FASLG, GAPDH, HMGB1, HMGB2, HSPA5, HSPA8, HSPA9, IFNG, IFNGR1, IFNGR2, IL5, IL13, IL13RA2, IL4, IRF2, IRF8, JUN, KTN1, MCF2L, MYL9, NDRG2, NFKB1, OPHN1, PAK2, PAK4, PDCD11, PIK3CA, PIK3CD, PIK3CG, PPP2R2A, PPP4C, PTEN, PRNP, RAC1, RAC2, RELA, RELB, RHOA, RNF34, ROCK1, RPS6KB1, RTKN, SIRT1, STAT6, TNF, TUBB, VAV3

Cluster 5 (Light Blue)	ASB1, ASB2, ASB4, ASB6, ASB7, ASB8, CFTR, CHEK2, COPS2, COPS3, COPS4, COPS5, COPS6, COPS8, CUL1, CUL2, CUL3, CUL5, DNAJA2, GPS1, HIF1A, IL2RB, LOC51035, SOCS1, SOCS3, SPTLC1, TCEB1, TCEB2, TP53, VCP, WSB1, ZER1
Cluster 6 (Yellow)	ADORA2A, ATP1A3, CYP27A1, DBH, F10, F2R, GJA1, GJA3, GRIN1, HAS2, HGF, HSD3B1, HSD3B2, IL1A, MUC4, NGFB, NQO2, PHOX2A, PLAT, PLA, PLG, SERPINB6, SERPINE1, SP1, SP3, SP4, SPHK1, TJP1

TABLE S4: Top 25 conserved miRNAs controlling the fibrosis network as ranked by spanning score (Related to Fig. 2). As we previously described (Bertero et al., 2014), spanning score considered (a) the fraction of network clusters targeted by each miRNA and (b) the hypergeometric p-value of the overlap of the target pool of the miRNA with the expanded fibrosis network. P-values were normalized by the theoretical maximum p-value, defined as the reciprocal of the number of simulations used to estimate the distribution (in this case, 100,000 simulations were used).

Rank	Score	Genes Targeted	Clusters Targeted	p-value	Family
1	3.000	40	6	0.0001	miR-181abcd/4262
2	2.875	35	6	0.0001	miR-29abcd
3	2.875	35	6	0.0001	miR-27abc/27a-3p
4	2.775	31	6	0.0001	miR-144
5	2.725	29	6	0.0001	miR-130ac/301ab/301b/301b-3p/454/721/4295/3666
6	2.675	27	6	0.0001	miR-410/344de/344b-1-3p
7	2.650	26	6	0.0001	miR-374ab
8	2.631	30	6	0.0003	miR-128/128ab
9	2.631	30	6	0.0003	let-7/98/4458/4500
10	2.550	22	6	0.0001	miR-221/222/222ab/1928
11	2.499	26	6	0.0004	miR-93/93a/105/106a/291a-3p/294/295/302abcde/372/373/428/519a/520be/520acd-3p/1378/1420ac
12	2.476	33	6	0.0025	miR-30abcdef/30abe-5p/384-5p
13	2.424	23	6	0.0004	miR-148ab-3p/152
14	2.405	27	6	0.0012	miR-300/381/539-3p
15	2.367	30	6	0.0034	miR-19ab
16	2.356	19	6	0.0003	miR-199ab-5p
17	2.327	30	6	0.0049	miR-17/17-5p/20ab/20b-5p/93/106ab/427/518a-3p/519d
18	2.300	22	6	0.0010	miR-145

Rank	Score	Genes Targeted	Clusters Targeted	p-value	Family
19	2.275	24	6	0.0020	miR-101/101ab
20	2.244	29	6	0.0084	miR-590-3p
21	2.240	32	6	0.0174	miR-340-5p
22	2.205	22	6	0.0024	miR-543
23	2.149	18	6	0.0016	miR-22/22-3p
24	2.117	21	6	0.0043	miR-202-3p
25	2.084	17	5	0.0005	miR-155

Supplemental Experimental Procedures

Network Construction

To construct the initial fibrosis network, we manually curated a set of 133 genes known fibrotic genes. Rather than compile a set of all genes known be modulated in fibrotic disease, we focused only on genes known to play a causative role in tissue fibrosis, through their involvement in matrix deposition and degradation, collagen crosslinking, and other fibrotic cellular processes. As previously described (Bertero et al., 2014), interactions between curated genes were annotated according to a master list of protein-protein, protein-DNA, kinase-substrate, and metabolic interactions, drawn from several consolidated databases, referred to here as the "consolidated interactome" (Parikh et al., 2012). In order to capture any additional fibrotic genes that may have been missed in our initial curation, we also incorporated a select number of non-curated genes demonstrated to interact with a significant number of genes in our curated set. As previously described (Bertero et al., 2014), this was performed by first defining a set of "fibrosis interactors." An interactor was defined as any node in the consolidated interactome that (a) directly interacted with at least one member of our curated fibrosis gene set, but (b) was not itself a member of the curated set. Fibrosis interactors were then iteratively ranked by their shortest-path betweenness centrality score, considering only shortest paths between genes defined as "fibrotic" (initially members of the curated fibrosis set). With each iteration, the highest scoring node was incorporated into the fibrosis network, and defined as "fibrotic" on the next iteration. As discussed below, this same method was used to expand each of the 137 disease-specific networks. In order to prevent comparison of excessively large datasets, when the normalized betweenness

centrality score of the highest scoring interactor fell below a fixed threshold of 0.10 (or, in the case of the disease-specific networks, when the number of incorporated nodes grew to twice the size of the original number of seed genes), no further nodes were added to the network. The resulting fibrosis network contained 350 nodes and 1459 edges, with a largest connected component of 339 nodes.

Network Clustering

Clustering was performed using the Louvain method for community detection (Blondel et al., 2008), as implemented in the NetworkX package for Python 3.3. The final partition was selected so as to maximize modularity in the graph.

miRNA Target Prediction

miRNA target prediction was performed using the TargetScan 6.2 (Conserved) algorithm (Friedman et al., 2009). The TargetScan algorithm detects mRNA with conserved complimentarity to the “seed” (nucleotides 2-7) of a given miRNA. Because of this, miRNA that share a seed are grouped together as a family and regarded as a single unit by the algorithm. For this reason, we do not distinguish between miRNA belonging to the same family in any of our statistical analyses.

miRNA Spanning Score

In order to rank the influence of miRNA families on the fibrosis network (and other disease networks), we ranked miRNAs based on their “spanning score” (see also Table S4). As previously described (Bertero et al., 2014), this metric scores a miRNA family on

three criteria: (1) the number of network genes which it targets, (2) the number of network clusters in which its targets reside, and (3) the hypergeometric p-value for the overlap of its target pool with the network. Each of these criteria is scored relatively, as a fraction of the maximum value achieved by any miRNA in our dataset for the network under consideration. This method provides a holistic assessment of the influence of a miRNA family on a given network of genes, considering not only the size, but also the spread and statistical significance of its target pool within the network.

Immunoblotting and antibodies

Cells were lysed in Laemmeli buffer. Protein lysate were resolved by SDS-PAGE and transferred onto a PVDF membrane (Biorad). Membranes were blocked in 5% non-fat milk in TN buffer (50 mM Tris-HCl pH 7.4, 150 mM NaCl) or 5% BSA in TN buffer and incubated in the presence of the primary and then secondary antibodies. After washing in TN buffer containing 0.1% Tween, immunoreactive bands were visualized with the ECL system (Amersham Biosciences). Primary antibodies for YAP (#8418; 1/1000), LATS1 (#9153, 1/1000), P-LATS1 (#9157, 1/1000), MST1 (#3682, 1/1000) and P-MST1/2 (#3681, 1/1000) were obtained from Cell Signaling. Primary antibodies for APOE (ab1906; 1/100), LRP8 (ab108208; 1/1000), and Actin (ab 3280; 1/500) were obtained from Abcam. Primary antibodies for YAP1 (sc-15407, 1/500) and TAZ (sc-48805, 1/250) were obtained from Santa Cruz Biotechnology. Appropriate secondary antibodies (anti-rabbit and anti-mouse) coupled to HRP were used (Santa Cruz Biotechnology).

Cell Culture and Reagents

Primary human pulmonary arterial adventitial fibroblast cells (PAAFs, Sciencell) were grown in FGM media (Lonza). Experiments were performed at passages 3-6. Primary human pulmonary arterial endothelial cells (PAECs) were grown in EGM-2 cell culture media (Lonza), and experiments were performed at passages 3 to 6. Primary human pulmonary arterial smooth muscle cells (PASMCs) were cultured in SmGM-2 cell culture media (Lonza), and experiments were performed at passages 3 to 9. HEK293T cells (American Type Culture Collection) were cultivated in DMEM containing 10% fetal bovine serum (FBS). All cells were grown in collagen-coated plastic (50ug/mL) at 37^{o}C in a humidified 5% CO_2 atmosphere. Collagen-coated hydrogel was purchased from Matrigen. Recombinant ApoE (PeproTech) was used at a concentration of 5 μM. Neutralizing antibody for FGF2 (05-117, Millipore) and IL-6 (ab6672, Abcam) were used at 2μg/mL. IgG isotype control antibody (Abcam) was used as control.

Plasmids

The 3'UTR sequences for LRP8 was purchased as gene fragment blocks (IDT) and cloned in the pSI-CHECK-2 vector (Promega) downstream of the Renilla luciferase using XhoI and NotI restrictions sites. Mutagenesis of the putative miR-130/301 family binding sites was performed using gene fragment blocks containing mutations in positions 2, 4, and 6 of the "seed" biding site (IDT). The PPARγ coding sequence (BC006811) was amplified by polymerase chain reaction (PCR) using high-fidelity polymerase Phusion (Thermo Fisher Scientific) from an MGC cDNA clone (clone ID: 3447380) and inserted in

the pCDH-CMV-MCS-EF1-copGFP (System Biosciences) using NheI and NotI restrictions sites. The YAP1 coding sequence was purchased (Addgene; Plasmid #18881) and sub-cloned in the pCDH-CMV-MCS-EF1-copGFP (System Biosciences) using EcoRI and NotI restriction sites. The lentiviral parent vector expressing GFP was used as a control. Stable expression of these constructs in PAAFs, PAECs, and PASMCs was achieved by lentiviral transduction. All cloned plasmids were confirmed by DNA sequencing.

Lentivirus production

HEK293T cells were transfected using Lipofectamine 2000 (Thermo Scientific) with lentiviral plasmids along with packaging plasmids (pPACK, System Biosciences), according to the manufacturer's instructions. Virus was harvested, sterile filtered (0.45 um), and utilized for subsequent infection of PAAFs, PAECs, and PASMCs (24-48 hour incubation) for gene transduction.

miRNA target validation by luciferase assay

Adapted from our previously published protocol, HEK293T cells were plated in 96-well plates and transfected with 200 ng of pSICHECK-2 construct and 5 nM of pre-miRNAs using Lipofectamine 2000 (Thermo Scientific). The medium was replaced 8 hours after transfection with fresh medium containing 10% FCS, L-glutamine. 48 hours after transfection, firefly and *Renilla* Luciferase activities were measured using the Dual-GloTM Luciferase assay (Promega).

Messenger RNA and miRNA extraction

Cells were homogenized in 1 ml of QiaZol reagent (Qiagen). Total RNA content, including small RNAs, was extracted using the miRNeasy kit (Qiagen) according to the manufacturer's instructions. Total RNA concentration was determined using a ND-1000 micro-spectrophotometer (NanoDrop Technologies).

Quantitative RT-PCR of mature miRNAs

Mature miRNA expression was evaluated using TaqMan MicroRNA Assays (Thermo Scientific/Applied Biosystems) and the Applied Biosystems 7900HT Fast Real Time PCR device (Thermo Scientific/Applied Biosystems). Expression levels were normalized to RNU48 or snoR55 for human or mouse experiments, respectively, and calculated using the comparative Ct method ($2^{-\Delta\Delta Ct}$).

Quantitative RT-PCR of messenger RNAs

Messenger RNAs were reverse transcribed using the Multiscript RT kit (Thermo Scientific) to generate cDNA. cDNA was amplified via fluorescently labeled Taqman primer sets using an Applied Biosystems 7900HT Fast Real Time PCR device. Fold-change of RNA species was calculated using the formula ($2^{-\Delta\Delta Ct}$), normalized to actin expression.

Immunofluorescence

After the different treatment cells were fixed with PBS/PFA 4% for 10 min and permeabilized with PBS/Triton 100X 0.1% for 10min. Then cells were incubated with

anti-YAP1 (#4912; 1/100; Cell signaling) at 4°C overnight. Secondary antibodies coupled with Alexa-594 (Thermo Scientific) were used at 1:500. Nuclei were counterstained with DAPI (Sigma).

BrdU proliferation assay

Exponentially growing cells were plated in the indicated matrix for 48 hours. For proliferation assays, 5-bromo-2-uridine (BrdU) was added to the cell culture medium for 1 hour, and BrdU incorporated into the DNA was revealed using a detection kit (BrdU Cell Proliferation Assay Kit #6813, Cell Signaling) according to the manufacturer's instructions.

ChIP-qPCR

PAAFs were cultivated on plastic for 48h. Cells were dual cross-linked with 2 mM disuccinimidyl glutarate (DSG) for 45 minutes and then in 1% paraformaldehyde for 15 minutes at room temperature. Fixed cells were lysed in 10 ml of Lysis Buffer 1 [50 mM HEPES (pH 7.5), 140 mM NaCl, 1 mM EDTA, 0.1% IGEPAL 630 (Sigma Aldrich)], containing 0.05% Triton X100, 2.5 % glycerol and supplemented with 1X protease inhibitor cocktail (Roche, Rotkreuz, Switzerland) for 10 minutes on ice, followed by incubation in Buffer 2 [0.1 M Tris HCl (pH 8) and 200 mM NaCl with protease inhibitors] for 15 minutes at room temperature. Chromatin was sonicated at 30% of amplitude for 10 minutes (10 cycles of 1 minute). The samples were centrifuged (2X 14,000 g for 5 minutes each), and soluble chromatin was transferred to a fresh tube. Crosslinked DNA after sonication was precipitated with 5 µg of anti-OCT4 antibody (ab19857, Abcam) or

non-immune rabbit IgG (ab27472, Abcam) overnight at 4°C. Chromatin/antibody complex was pulled down with PureProteome™ Protein G Magnetic Beads (Millipore) and washed in the low- and high-salt buffers. After crosslinking reversion (65°C for 4 hours) and Proteinase K treatment, chromatin was purified by phenol-chloroform extraction and ethanol precipitation. Precipitated DNA was analyzed by qPCR using primers generated for predicted Oct4 binding sites in the promoters of the miR-130/301 family members. Control primers were generated corresponding to the downstream genomic regions, corresponding to the coding sequences for the primary miRNA transcripts of each miR-130/301 family member (Control).

Three-dimensional cell culture

This protocol was adapted from a prior publication (Aragona et al., 2013). Cells were embedded in a mixture of Growth Factor Reduced Matrigel (BD Biosciences) and Collagen-I (BD Biosciences). Collagen-I solution was neutralized on ice with 0.1M NaOH in PBS and adjusted with 0.1N HCl to bring the pH of the solution to 7.5. The Collagen-I solution was then mixed on ice with Matrigel to obtain a final concentration of 1.2 mg/ml (soft matrix) or 3 mg/ml (stiff matrix). Cells were trypsinized, counted, and resuspended in growth medium. 1:1 (v/v) mixtures were generated of cells with ECM mixture. 6-well plates were pre-coated with 1 ml of cell-free 50% medium/50% ECM, followed by solidification of the gel at 37^{o}C in a humidified 5% CO_2 atmosphere. Cells were then seeded on the ECM gel. Subsequently, wells were supplemented with normal growth medium 0.5% FBS, which was changed every 2 days during experimentation.

ECM remodeling experiment

Following treatment, PAAFs were plated atop soft matrices in normal growth medium supplemented with 0.5% FBS. After three days, 10ug/mL of puromycin was added to the growth medium for 48 hours to detach the cells from the matrix. Matrices were washed 3 times (PBS). Naïve PAAFs were then plated on top of these matrices supplemented with normal growth medium 0.5% FBS or harvested for assessment of fibrillar collagen content (Picrosirius Red stain). Sixteen hours later, cells were harvested for immunofluorescence experiments or RNA extraction.

Measurement of collagen content in lung tissue

This protocol was adapted from a previously published protocol (Hu et al.). Mouse lung was weighed, minced, and incubated in 0.5 M acetic acid at 4^{o}C. After overnight digestion, the acetic acid-soluble and insoluble fractions were isolated by centrifugation. The soluble fraction was stored at -80^{o}C, while the insoluble fraction was digested by overnight incubation in 6M hydrochloric acid at 85^{o}C. Concentrations of soluble and insoluble (gelatinous) collagen fractions were determined using a Sircol Soluble Collagen Assay Kit (Biocolor) with a colorimetric reaction (measured at 550 nm) and a collagen reference standard curve**.**

LOX activity assay

Lox activity was measured using the Lysyl Oxidase Activity Assay Kit (Ab112139), following the manufacturer instructions. Briefly, 50μl of conditioned phenol-red-free medium was taken from cells incubated for 48h in the indicated condition. Media was

incubated for 30min in presence of 50uL of reaction mixture +/- 500μM BAPN. Fluorescence was monitored with a fluorescence plate reader at Ex/Em = 540/590 nm and fluorescence (a measure of LOX activity) was plotted, where 0 = sample + 500 μM BAPN (complete LOX inhibition). For analysis of *in vivo* specimens, 5μg of total protein extracts from whole lung were analyzed. Again, 0 = fluorescent reading for 500μM BAPN.

Animals

All animal treatments and analyses were conducted in a controlled and non-blinded manner. *Pulmonary hypertension models*

- Eight-week-old littermate mice (C57Bl6) were exposed serially to SU5416 or vehicle control (20 mg/kg/dose/week; Sigma-Aldrich), followed by exposure to normobaric hypoxia (10% O2; OxyCycler chamber, Biospherix Ltd, Redfield, NY) or normoxia (21% O2) for 3 weeks.
- Male Sprague-Dawley rats (10-14 week old) were injected with 60 mg/kg monocrotaline at time 0. At 0-4 weeks post-exposure, right heart catheterization was performed followed by harvest of lung tissue for RNA extraction or paraffin embedding.
- VHL flox/flox;Cre-ER mice (C57Bl6 background, >10 backcrosses) were a generous gift from W.G. Kaelin (Dana Farber Cancer Institute, Boston). Conditional inactivation of VHL was performed by treating 3-week-old *VHL flox/flox*, *Cre-ER* mice with 2 mg of tamoxifen (Sigma Aldrich), administered via intraperitoneal injection every other day for 2 doses, as previously described (Chan et al., 2009),

followed by tissue harvest at 10-13 weeks of age. Tissue from tamoxifen-treated, gender- (male), and age-matched *VHL flox/flox* mice (without the Cre-ER transgene) was used as wildtype comparison (referred to as VHL WT).

- IL-6 transgenic mice (C57Bl6 background) have been described previously (Steiner et al., 2009).
- *Schistosoma mansoni*-infected mice: Mice were exposed to *S. mansoni* ova to cause experimental PH, using a published technique (Graham et al., 2013a; Graham et al., 2013b). Eight week old C57Bl6/J mice were used for the study. Experimentally exposed mice were intraperitoneally sensitized on day one and then intravenously challenged on day 14 with *S. mansoni* eggs, at a dose of 175 eggs/gram body weight at each time point. S. mansoni eggs were obtained from homogenized and purified livers of Swiss-Webster mice infected with *S. mansoni* cercariae, provided by the Biomedical Research Institute (Rockville, MD). On day 21, right ventricular catheterization was performed followed by tissue and blood collection. The mice were anesthetized with ketamine/xylazine and ventilated through a transtracheal catheter. The abdominal and thoracic cavities were opened, and a 1Fr pressure-volume catheter (Millar PVR-1035, Millar Instruments) was placed through the right ventricle apex to transduce the pressure. Blood samples (400μl) were drawn after catheterization using into a syringe containing 100 μL 0.5M EDTA at pH 8.0. Blood samples were centrifuged at 2000g for 20 minutes at 4°C to separate plasma. The remaining blood was flushed out of the lungs with PBS, the right bronchus was sutured, and 1% agarose was instilled into the left lung through the transtracheal catheter. The left lung was removed, formalin-fixed, and paraffin-embedded for

histology. The right lungs were removed and snap frozen. The right ventricle free wall was dissected off of the heart and weighed relative to the septum and left ventricle to measure hypertrophy (the Fulton index).

- Male Sprague-Dawley rats (10-14 week old) were injected with SU5416 (20 mg/kg; Sigma-Aldrich), followed by exposure to normobaric hypoxia (10% O2; OxyCycler chamber, Biospherix Ltd, Redfield, NY) or normoxia (21% O2) for 3 weeks. Right heart catheterization was performed, followed by harvest of lung tissue for RNA extraction or paraffin embedding.
- Surgical placement of PA-aortic shunts in juvenile lambs: As previously described (Reddy et al., 1995), pregnant mixed-breed Western ewes (137-141 d gestation, term = 145 d) were anesthetized. Fetal exposure was obtained through the horn of the uterus; a left lateral thoracotomy was performed on the fetal lamb. With the use of side-biting vascular clamps, an 8.0-mm vascular graft was anastomosed between the ascending aorta and main pulmonary artery of the fetal lambs. Four weeks after spontaneous delivery shunt and control (provided by twin pregnancy or age-matched) lambs were anesthetized and catheters were placed to measure hemodynamics including left pulmonary blood flow. After baseline hemodynamics were obtained, peripheral lung was obtained for analysis. At the end of the protocol, all lambs were euthanized with a lethal injection of sodium pentobarbital followed by bilateral thoracotomy as described in the National Institutes of Health Guidelines for the Care and Use of Laboratory Animals.

Lung tissue harvest

After physiological measurements by direct right ventricular puncture, the pulmonary vessels were gently flushed with 1 cc of saline to remove the majority of blood cells, prior to harvesting cardiopulmonary tissue. The heart was removed, followed by dissection and weighing of the right ventricle (RV) and of the left ventricle + septum (LV+S). Organs were then harvested for histological preparation or flash frozen in liquid N2 for subsequent homogenization and extraction of RNA and/or protein. To further process lung tissue specifically, prior to excision, lungs were flushed with PBS at constant low pressure (~10mmHg) via right ventricular cannulation, followed by tracheal inflation of the left lung with 10% neutral-buffered formalin (Sigma-Aldrich) at a pressure of ~20cm H_2O. After excision and 16 hours of fixation in 10% neutral-buffered formalin at 25^{o}C, lung tissues were paraffin-embedded via an ethanol-xylene dehydration series, before being sliced into 5µm sections (Hypercenter XP System and Embedding Center, Shandon).

Atomic force microscopy

Adapted from a prior protocol in rodent lung (Liu et al., 2015), mouse lungs were inflated with OCT (0.05mL/g), frozen and cut into 40µm thick sections for atomic force microscopy (AFM) analysis. AFM (MFP-3D; Asylum Research) was used to mechanically characterize peripheral pulmonary arterioles (smaller than 50µm in diameter) by performing microindentation using a cantilever with a spring constant of ~60 pN/nm and a sphere tip with a diameter of 5 µm (Novascan). A total of 9 vessels were analyzed per animal (n=4 per group). For each vessel, 3 measurements were made at different locations within the media of each vessel. Force-indentation profiles

were acquired at an indentation rate of 20 μm/s and the shear modulus was calculated by fitting force-indentation data using a Hertz sphere model.

In situ hybridization

The protocol for *in situ* hybridization for miRNA detection was based on a prior report (Bertero et al., 2014). Specifically, 5μm tissues sections were probed using a 3' fluorescein isothiocyanate (FITC) labeled miRCURY LNA hsa-miR-130a detection probe (Exiqon). The miRCURY LNA scramble-miR probe was used as negative control. Following re-hydration (Sigma) tissues were formaldehyde-fixed (4% formaldehyde, Sigma) before inactivation of endogenous enzymes by acetylation buffer [873 uL of triethanolamine (Sigma) and 375 uL acetic anhydride (Fisher) in 75 ml distilled water]. Probe annealing (25 nM LNA probe) was performed in hybridization buffer (Sigma, H7782) for 16 hours at RNA-Tm-22°C (62^{o}C). Following serial washes with 2X SSC, 1X SSC, and 0.5X SSC (Sigma) at 62^{o}C, immunolabeling was performed with an anti-FITC biotin conjugated antibody for overnight at 4^{o}C (1:400; Sigma-Aldrich). For detection, development was achieved by adding streptavidin-biotinylated alkaline phosphatase complex (Vector Labs) followed by Nitro blue tetrazolium chloride/5-Bromo–4-chloro–3–indolyl phosphate substrate solution (NBT/BCIP, Roche), and positive staining was evident by a blue color. MiR-130a expression was quantified in the vascular wall of 15-20 pulmonary arteries (<100μm external diameter in rodents and <200μm external diameter in humans) using ImageJ software (NIH).

Picrosirius Red stain and quantification

Picrosirius Red stain was achieved through the use of 5μm paraffin sections stained with 0.1% Picrosirius Red (Direct Red80, Sigma-Aldrich) and counterstained with Weigert's hematoxylin to reveal fibrillar collagen. The sections were then serially imaged using with an analyzer and polarizer oriented parallel and orthogonal to each other. Microscope conditions (lamp brightness, condenser opening, objective, zoom, exposure time, and gain parameters) were constant throughout the imaging of all samples. A minimal threshold was set on appropriate control sections for each experiment in which only the light passing through the orthogonally-oriented polarizers representing fibrous structures (*i.e.*, excluding residual light from the black background) was included. The threshold was maintained for all images across all conditions within each experiment. The area of the transferred regions that was covered by the thresholded light was calculated and at least 10 sections/vessel per condition were averaged together (Image J software).

Immunohistochemistry and immunofluorescence of lung sections

Lung sections (5μm) were deparaffinized and high temperature antigen retrieval was performed, followed by blocking in TBS/BSA 5%, 10% goat serum and exposure to primary antibody and biotinylated secondary antibody (Vectastain ABC kit, Vector Labs) for immunohistochemistry or Alexa 488, 568 and 647-conjugated secondary antibodies (Thermo Fisher Scientific) for immunofluorescence. A primary antibody against YAP1 (#4912; 1/200) was obtained from Cell Signaling. Primary antibodies against, LRP8 (ab115196; 1/100), LOX (ab31238; 1/100) and α-SMA (1/400) were purchased from Abcam. Primary antibodies against OCT4 (sc-5279; 1/50), CD31 (sc-1506; 1/100), and PPARγ (sc-7273; 1/50) were purchased from Santa Cruz Biotechnology. A primary

antibody against PCNA (13-3900, 1/100) was purchased from Thermo Fisher Scientific. Primary antibody against anti-shortmer (E5746-B3A; 1/1000) was provided by Regulus Therapeutics. In most cases, color development was achieved by adding streptavidin-biotinylated alkaline phosphatase complex (Vector Labs) followed by Vector Red alkaline phosphatase substrate solution (Vector Labs). Levamisole was added to block endogenous alkaline phosphatase activity (Vector Labs). Pictures were obtained using an Olympus Bx51 microscope or ZEISS LSM Exciter confocal microscope (405nm/488nm/543nm/633nm wavelengths). Small pulmonary vessels (<100 □m diameter) present in a given tissue section (>10 vessels/section) that were not associated with bronchial airways were selected for analysis (N>5 animals/group). Intensity of staining was quantified using ImageJ software (NIH). Degree of pulmonary arteriolar muscularization was assessed in paraffin-embedded lung sections stained for α–SMA by calculation of the proportion of fully and partially muscularized peripheral (<100 μm diameter) pulmonary arterioles to total peripheral pulmonary arterioles, as previously described (Hansmann et al., 2007). Medial thickness was also measured in α–SMA stained vessels (<100 μm diameter) using ImageJ software (NIH) and expressed as arbitrary units. All measurements were performed blinded to condition.

RNA-Sequencing

The Illumina TruSeq RNA Sample Preparation v2 kit was used to construct libraries for the samples accordingly to the manufacturer protocol. Briefly, 150ng of total RNA input was used. The libraries were quantified using KAPA library quantification kit.
Unstranded, paired-end sequencing was then done on Illumina HiSeq 2000 at 50 cycles/base-pair to generate 50bp paired-end reads. Around 14 ~ 19 million reads per

sample were generated. Experimental data and associated designs were deposited in the NCBI Gene Expression Omnibus (http://www.ncbi.nlm.nih.gov/geo/) under series GSE61828.

RNA-Seq data pre-processing and analysis

FastQC(FastQC), a quality control tool for high throughput sequence data, was used for checking q-scores and reads were not trimmed prior to alignments. The data were aligned against UCSC mouse genome version mm10 using STAR aligner (Dobin et al., 2013). Then, from the BAM files, gene-level counts of uniquely mapped reads were computed using SAMTools (Li et al., 2009a) and HTSeq v0.5.4p5 (Smyth et al., 2005). The gene level counts were then normalized with the R/Bioconductor package limma(Smyth et al., 2005) using the voom(Law et al., 2014)/variance stabilization method. The data were quality controlled for outliers using principal component analysis (PCA). Differential expression analysis between transcriptome profiles of experimental groups was performed using the R / Bioconductor package limma(Smyth et al., 2005) that includes methods for RNA-Seq Data analysis.

Statistical analysis: Transcriptomic analysis was performed in the lungs of mice exposed to hypoxia + SU5416 and treated with either Short-NC (n=3) or Short-130 (n=3) as described above, as compared with mice exposed to normoxia + SU5416. Genes that showed robust modulation in the context of hypoxia ($p<0.05$) and modulation in the opposite direction when miR-130/301 was suppressed ($p<0.15$) were cross-referenced with the consolidated interactome (CI) to form a network whose modulation under

hypoxia was miR-130/301-dependent. Notably, we chose to use a less stringent p-value cutoff for modulation under conditions of miR-130/301 suppression, as these genes had already been subject to two prior screening criteria: (1) they were modulated in the context of hypoxia ($p<0.05$) and (2) hypoxia-induced effects were reversed when miR-130/301 was suppressed. As we believed these criteria to be fairly stringent on their own, we felt it was unnecessary to exclude genes with moderately low p-values if they met these other specifications.

Pathway Enrichment: Pathway enrichment of this network was performed using the Reactome FI plug-in for Cytoscape 2.0. The network was cross-referenced with several databases (Kegg, Reactome, GO, NCBI PID, and Biocarta) collectively representing a broad range of functional pathways. Pathways were then ranked according to the hypergeometric p-value for their overlap with this miR-130/301-dependent network (as we have previously described (Parikh et al., 2012)).

Target analysis. De-repression of miR-130/301 target genes by Short-130 administration was assessed using the sylamer approach (van Dongen et al., 2008) as previously reported (Bertero et al., 2014).

Supplemental References

Antsiferova, M., and Werner, S. (2012). The bright and the dark sides of activin in wound healing and cancer. J Cell Sci *125*, 3929-3937.

Aragona, M., Panciera, T., Manfrin, A., Giulitti, S., Michielin, F., Elvassore, N., Dupont, S., and Piccolo, S. (2013). A mechanical checkpoint controls multicellular growth through YAP/TAZ regulation by actin-processing factors. Cell *154*, 1047-1059.

Avouac, J., Palumbo, K., Tomcik, M., Zerr, P., Dees, C., Horn, A., Maurer, B., Akhmetshina, A., Beyer, C., Sadowski, A.*, et al.* (2012). Inhibition of activator protein 1 signaling abrogates transforming growth factor beta-mediated activation of fibroblasts and prevents experimental fibrosis. Arthritis Rheum *64*, 1642-1652.

Baghy, K., Dezso, K., Laszlo, V., Fullar, A., Peterfia, B., Paku, S., Nagy, P., Schaff, Z., Iozzo, R.V., and Kovalszky, I. (2011). Ablation of the decorin gene enhances experimental hepatic fibrosis and impairs hepatic healing in mice. Lab Invest *91*, 439-451.

Barry-Hamilton, V., Spangler, R., Marshall, D., McCauley, S., Rodriguez, H.M., Oyasu, M., Mikels, A., Vaysberg, M., Ghermazien, H., Wai, C.*, et al.* (2010). Allosteric inhibition of lysyl oxidase-like-2 impedes the development of a pathologic microenvironment. Nat Med *16*, 1009-1017.

Bartlett, J.R., Friedman, K.J., Ling, S.C., Pace, R.G., Bell, S.C., Bourke, B., Castaldo, G., Castellani, C., Cipolli, M., Colombo, C.*, et al.* (2009). Genetic modifiers of liver disease in cystic fibrosis. JAMA *302*, 1076-1083.

Bayle, J., Fitch, J., Jacobsen, K., Kumar, R., Lafyatis, R., and Lemaire, R. (2008). Increased expression of Wnt2 and SFRP4 in Tsk mouse skin: role of Wnt signaling in altered dermal fibrillin deposition and systemic sclerosis. J Invest Dermatol *128*, 871-881.

Bedford, J.J., Leader, J.P., and Walker, R.J. (2003). Aquaporin expression in normal human kidney and in renal disease. J Am Soc Nephrol *14*, 2581-2587.

Besnard, A.G., Struyf, S., Guabiraba, R., Fauconnier, L., Rouxel, N., Proost, P., Uyttenhove, C., Van Snick, J., Couillin, I., and Ryffel, B. (2013). CXCL6 antibody neutralization prevents lung inflammation and fibrosis in mice in the bleomycin model. J Leukoc Biol *94*, 1317-1323.

Blondel, V.D., Guillaume, J.L., Hendrickx, J.M., de Kerchove, C., and Lambiotte, R. (2008). Local leaders in random networks. Phys Rev E Stat Nonlin Soft Matter Phys *77*, 036114.

Bonilla, N., Barget, N., Andrieu, M., Roulot, D., Letoumelin, P., Grando, V., Trinchet, J.C., Ganne-Carrie, N., Beaugrand, M., Deny, P.*, et al.* (2006). Interferon gamma-secreting HCV-specific CD8+ T cells in the liver of patients with chronic C hepatitis: relation to liver fibrosis--ANRS HC EP07 study. J Viral Hepat *13*, 474-481.

Bonner, J.C. (2004). Regulation of PDGF and its receptors in fibrotic diseases. Cytokine Growth Factor Rev *15*, 255-273.

Boon, M.R., van der Horst, G., van der Pluijm, G., Tamsma, J.T., Smit, J.W., and Rensen, P.C. (2011). Bone morphogenetic protein 7: a broad-spectrum growth factor with multiple target therapeutic potency. Cytokine Growth Factor Rev *22*, 221-229.

Bopp, A., Wartlick, F., Henninger, C., Kaina, B., and Fritz, G. (2013). Rac1 modulates acute and subacute genotoxin-induced hepatic stress responses, fibrosis and liver aging. Cell Death Dis *4*, e558.

Boutet, A., De Frutos, C.A., Maxwell, P.H., Mayol, M.J., Romero, J., and Nieto, M.A. (2006). Snail activation disrupts tissue homeostasis and induces fibrosis in the adult kidney. EMBO J *25*, 5603-5613.

Brilla, C.G., Reams, G.P., Maisch, B., and Weber, K.T. (1993). Renin-angiotensin system and myocardial fibrosis in hypertension: regulation of the myocardial collagen matrix. Eur Heart J *14 Suppl J*, 57-61.

Chakraborty, S., Chopra, P., Hak, A., Dastidar, S.G., and Ray, A. (2013). Hepatocyte growth factor is an attractive target for the treatment of pulmonary fibrosis. Expert Opin Investig Drugs *22*, 499-515.

Chan, S.Y., Zhang, Y.Y., Hemann, C., Mahoney, C.E., Zweier, J.L., and Loscalzo, J. (2009). MicroRNA-210 controls mitochondrial metabolism during hypoxia by repressing the iron-sulfur cluster assembly proteins ISCU1/2. Cell Metab *10*, 273-284.

Checa, M., Ruiz, V., Montano, M., Velazquez-Cruz, R., Selman, M., and Pardo, A. (2008). MMP-1 polymorphisms and the risk of idiopathic pulmonary fibrosis. Hum Genet *124*, 465-472.

Corchero, J., Martin-Partido, G., Dallas, S.L., and Fernandez-Salguero, P.M. (2004). Liver portal fibrosis in dioxin receptor-null mice that overexpress the latent transforming growth factor-beta-binding protein-1. Int J Exp Pathol *85*, 295-302.

de Almeida, C.J., Jasmin, J.F., Del Galdo, F., and Lisanti, M.P. (2013). Genetic ablation of caveolin-2 sensitizes mice to bleomycin-induced injury. Cell Cycle *12*, 2248-2254.

De Minicis, S., Rychlicki, C., Agostinelli, L., Saccomanno, S., Trozzi, L., Candelaresi, C., Bataller, R., Millan, C., Brenner, D.A., Vivarelli, M*., et al.* (2013). Semaphorin 7A contributes to TGF-beta-mediated liver fibrogenesis. Am J Pathol *183*, 820-830.

Della Latta, V., Cabiati, M., Rocchiccioli, S., Del Ry, S., and Morales, M.A. (2013). The role of the adenosinergic system in lung fibrosis. Pharmacol Res *76*, 182-189.

Dobin, A., Davis, C.A., Schlesinger, F., Drenkow, J., Zaleski, C., Jha, S., Batut, P., Chaisson, M., and Gingeras, T.R. (2013). STAR: ultrafast universal RNA-seq aligner. Bioinformatics *29*, 15-21.

FastQC http://www.bioinformatics.babraham.ac.uk/projects/fastqc/.

Fern, R.J., Yesko, C.M., Thornhill, B.A., Kim, H.S., Smithies, O., and Chevalier, R.L. (1999). Reduced angiotensinogen expression attenuates renal interstitial fibrosis in obstructive nephropathy in mice. J Clin Invest *103*, 39-46.

Gao, X., Wang, G., Zhang, W., Peng, Q., Xue, M., and Jinhong, H. (2013). Expression of pulmonary aquaporin 1 is dramatically upregulated in mice with pulmonary fibrosis induced by bleomycin. Arch Med Sci *9*, 916-921.

Garcia-Prieto, E., Gonzalez-Lopez, A., Cabrera, S., Astudillo, A., Gutierrez-Fernandez, A., Fanjul-Fernandez, M., Batalla-Solis, E., Puente, X.S., Fueyo, A., Lopez-Otin, C*., et al.* (2010). Resistance to bleomycin-induced lung fibrosis in MMP-8 deficient mice is mediated by interleukin-10. PLoS One *5*, e13242.

Gervasi, M., Bianchi-Smiraglia, A., Cummings, M., Zheng, Q., Wang, D., Liu, S., and Bakin, A.V. (2012). JunB contributes to Id2 repression and the epithelial-mesenchymal transition in response to transforming growth factor-beta. J Cell Biol *196*, 589-603.

Gharaee-Kermani, M., McGarry, B., Lukacs, N., Huffnagle, G., Egan, R.W., and Phan, S.H. (1998). The role of IL-5 in bleomycin-induced pulmonary fibrosis. J Leukoc Biol *64*, 657-666.

Ghosh, A.K., Quaggin, S.E., and Vaughan, D.E. (2013). Molecular basis of organ fibrosis: potential therapeutic approaches. Exp Biol Med (Maywood) *238*, 461-481.

Ghosh, A.K., and Vaughan, D.E. (2012). PAI-1 in tissue fibrosis. J Cell Physiol *227*, 493-507.

Gieling, R.G., Wallace, K., and Han, Y.P. (2009). Interleukin-1 participates in the progression from liver injury to fibrosis. Am J Physiol Gastrointest Liver Physiol *296*, G1324-1331.

Goodman, S.L., and Picard, M. (2012). Integrins as therapeutic targets. Trends Pharmacol Sci *33*, 405-412.

Graham, B.B., Chabon, J., Gebreab, L., Poole, J., Debella, E., Davis, L., Tanaka, T., Sanders, L., Dropcho, N., Bandeira, A*., et al.* (2013a). Transforming growth factor-beta signaling promotes pulmonary hypertension caused by Schistosoma mansoni. Circulation *128*, 1354-1364.

Graham, B.B., Chabon, J., Kumar, R., Kolosionek, E., Gebreab, L., Debella, E., Edwards, M., Diener, K., Shade, T., Bifeng, G*., et al.* (2013b). Protective role of IL-6 in vascular remodeling in Schistosoma pulmonary hypertension. Am J Respir Cell Mol Biol *49*, 951-959.

Granel, B., Chevillard, C., and Dessein, A. (2007). [Interleukin 13 and interleukin 13 receptor involvement in systemic sclerosis]. Rev Med Interne *28*, 613-622.

Greenlee, K.J., Werb, Z., and Kheradmand, F. (2007). Matrix metalloproteinases in lung: multiple, multifarious, and multifaceted. Physiol Rev *87*, 69-98.

Grygielko, E.T., Martin, W.M., Tweed, C., Thornton, P., Harling, J., Brooks, D.P., and Laping, N.J. (2005). Inhibition of gene markers of fibrosis with a novel inhibitor of transforming growth factor-beta type I receptor kinase in puromycin-induced nephritis. J Pharmacol Exp Ther *313*, 943-951.

Guo, Y., Xiao, L., Sun, L., and Liu, F. (2012). Wnt/beta-catenin signaling: a promising new target for fibrosis diseases. Physiol Res *61*, 337-346.

Gvaramia, D., Blaauboer, M.E., Hanemaaijer, R., and Everts, V. (2013). Role of caveolin-1 in fibrotic diseases. Matrix Biol *32*, 307-315.

Hansmann, G., Wagner, R., Schellong, S., Perez, V., Urashima, T., Wang, L., Sheikh, A., Suen, R., Stewart, D., and Rabinovitch, M. (2007). Pulmonary arterial hypertension is linked to insulin resistance and reversed by peroxisome proliferator-activated receptor-gamma activation. Circulation *115*, 1275-1284.

Hu, B., Castillo, E., Harewood, L., Ostano, P., Reymond, A., Dummer, R., Raffoul, W., Hoetzenecker, W., Hofbauer, G.F., and Dotto, G.P. (2012a). Multifocal epithelial tumors and field cancerization from loss of mesenchymal CSL signaling. Cell *149*, 1207-1220.

Hu, B., Wu, Z., Nakashima, T., and Phan, S.H. (2012b). Mesenchymal-specific deletion of C/EBPbeta suppresses pulmonary fibrosis. Am J Pathol *180*, 2257-2267.

Huang, L.S., Berdyshev, E., Mathew, B., Fu, P., Gorshkova, I.A., He, D., Ma, W., Noth, I., Ma, S.F., Pendyala, S.*, et al.* (2013). Targeting sphingosine kinase 1 attenuates bleomycin-induced pulmonary fibrosis. FASEB J *27*, 1749-1760.

Huang, X.Z., Wen, D., Zhang, M., Xie, Q., Ma, L., Guan, Y., Ren, Y., Chen, J., and Hao, C.M. (2014). Sirt1 activation ameliorates renal fibrosis by inhibiting the TGF-beta/Smad3 pathway. J Cell Biochem *115*, 996-1005.

Humphreys, B.D., Xu, F., Sabbisetti, V., Grgic, I., Naini, S.M., Wang, N., Chen, G., Xiao, S., Patel, D., Henderson, J.M.*, et al.* (2013). Chronic epithelial kidney injury molecule-1 expression causes murine kidney fibrosis. J Clin Invest *123*, 4023-4035.

Jeong, W.I., Park, O., Radaeva, S., and Gao, B. (2006). STAT1 inhibits liver fibrosis in mice by inhibiting stellate cell proliferation and stimulating NK cell cytotoxicity. Hepatology *44*, 1441-1451.

Jiang, D., Liang, J., Campanella, G.S., Guo, R., Yu, S., Xie, T., Liu, N., Jung, Y., Homer, R., Meltzer, E.B.*, et al.* (2010). Inhibition of pulmonary fibrosis in mice by CXCL10 requires glycosaminoglycan binding and syndecan-4. J Clin Invest *120*, 2049-2057.

Kajdaniuk, D., Marek, B., Borgiel-Marek, H., and Kos-Kudla, B. (2011). Vascular endothelial growth factor (VEGF) - part 1: in physiology and pathophysiology. Endokrynol Pol *62*, 444-455.

Kim, W., Moon, S.O., Lee, S.Y., Jang, K.Y., Cho, C.H., Koh, G.Y., Choi, K.S., Yoon, K.H., Sung, M.J., Kim, D.H.*, et al.* (2006). COMP-angiopoietin-1 ameliorates renal fibrosis in a unilateral ureteral obstruction model. J Am Soc Nephrol *17*, 2474-2483.

Kisseleva, T., and Brenner, D.A. (2011). Anti-fibrogenic strategies and the regression of fibrosis. Best Pract Res Clin Gastroenterol *25*, 305-317.

Kum, Y.S., Kim, K.H., Park, T.I., Suh, I.S., Oh, H.K., Cho, C.H., Park, J.B., Chang, Y.C., Park, J.H., Lee, K.G.*, et al.* (2007). Antifibrotic effect via the regulation of transcription factor Sp1 in lung fibrosis. Biochem Biophys Res Commun *363*, 368-374.

Lai, C.F., Lin, S.L., Chiang, W.C., Chen, Y.M., Wu, V.C., Young, G.H., Ko, W.J., Kuo, M.L., Tsai, T.J., and Wu, K.D. (2014). Blockade of Cysteine-rich Protein 61 Attenuates Renal Inflammation and Fibrosis after Ischemic Kidney Injury. Am J Physiol Renal Physiol.

Lam, A.P., Herazo-Maya, J.D., Sennello, J.A., Flozak, A.S., Russell, S., Mutlu, G.M., Budinger, G.R., DasGupta, R., Varga, J., Kaminski, N.*, et al.* (2014). Wnt coreceptor lrp5 is a driver of idiopathic pulmonary fibrosis. Am J Respir Crit Care Med *190*, 185-195.

Lan, H.Y. (2011). Diverse roles of TGF-beta/Smads in renal fibrosis and inflammation. Int J Biol Sci *7*, 1056-1067.

Law, C.W., Chen, Y., Shi, W., and Smyth, G.K. (2014). voom: precision weights unlock linear model analysis tools for RNA-seq read counts. Genome Biol *15*, R29.

Li, H., Handsaker, B., Wysoker, A., Fennell, T., Ruan, J., Homer, N., Marth, G., Abecasis, G., and Durbin, R. (2009a). The Sequence Alignment/Map format and SAMtools. Bioinformatics *25*, 2078-2079.

Li, Y., Tan, X., Dai, C., Stolz, D.B., Wang, D., and Liu, Y. (2009b). Inhibition of integrin-linked kinase attenuates renal interstitial fibrosis. J Am Soc Nephrol *20*, 1907-1918.

Liedtke, C.M. (1992). Electrolyte transport in the epithelium of pulmonary segments of normal and cystic fibrosis lung. FASEB J *6*, 3076-3084.

Liu, S., Parapuram, S.K., and Leask, A. (2013). Fibrosis caused by loss of PTEN expression in mouse fibroblasts is crucially dependent on CCN2. Arthritis Rheum *65*, 2940-2944.

Liu, W., Ding, I., Chen, K., Olschowka, J., Xu, J., Hu, D., Morrow, G.R., and Okunieff, P. (2006). Interleukin 1beta (IL1B) signaling is a critical component of radiation-induced skin fibrosis. Radiat Res *165*, 181-191.

Lopez, B., Gonzalez, A., Hermida, N., Valencia, F., de Teresa, E., and Diez, J. (2010). Role of lysyl oxidase in myocardial fibrosis: from basic science to clinical aspects. Am J Physiol Heart Circ Physiol *299*, H1-9.

Madala, S.K., Schmidt, S., Davidson, C., Ikegami, M., Wert, S., and Hardie, W.D. (2012). MEK-ERK pathway modulation ameliorates pulmonary fibrosis associated with epidermal growth factor receptor activation. Am J Respir Cell Mol Biol *46*, 380-388.

Maher, T.M. (2012). Idiopathic pulmonary fibrosis: pathobiology of novel approaches to treatment. Clin Chest Med *33*, 69-83.

Mandal, P., Pritchard, M.T., and Nagy, L.E. (2010). Anti-inflammatory pathways and alcoholic liver disease: role of an adiponectin/interleukin-10/heme oxygenase-1 pathway. World J Gastroenterol *16*, 1330-1336.

Mangieri, D., Corradi, D., Martorana, D., Malerba, G., Palmisano, A., Libri, I., Bartoli, V., Carnevali, M.L., Goldoni, M., Govoni, P.*, et al.* (2012). Eotaxin/CCL11 in idiopathic retroperitoneal fibrosis. Nephrol Dial Transplant *27*, 3875-3884.

Margadant, C., and Sonnenberg, A. (2010). Integrin-TGF-beta crosstalk in fibrosis, cancer and wound healing. EMBO Rep *11*, 97-105.

Maring, J.A., Trojanowska, M., and ten Dijke, P. (2012). Role of endoglin in fibrosis and scleroderma. Int Rev Cell Mol Biol *297*, 295-308.

Miao, C.G., Yang, Y.Y., He, X., Huang, C., Huang, Y., Zhang, L., Lv, X.W., Jin, Y., and Li, J. (2013). Wnt signaling in liver fibrosis: progress, challenges and potential directions. Biochimie *95*, 2326-2335.

Murphy, M., McMahon, R., Lappin, D.W., and Brady, H.R. (2002). Gremlins: is this what renal fibrogenesis has come to? Exp Nephrol *10*, 241-244.

Oakley, F., Mann, J., Nailard, S., Smart, D.E., Mungalsingh, N., Constandinou, C., Ali, S., Wilson, S.J., Millward-Sadler, H., Iredale, J.P.*, et al.* (2005). Nuclear factor-kappaB1 (p50) limits the inflammatory and fibrogenic responses to chronic injury. Am J Pathol *166*, 695-708.

Ogata, H., Chinen, T., Yoshida, T., Kinjyo, I., Takaesu, G., Shiraishi, H., Iida, M., Kobayashi, T., and Yoshimura, A. (2006). Loss of SOCS3 in the liver promotes fibrosis by enhancing STAT3-mediated TGF-beta1 production. Oncogene *25*, 2520-2530.

Olsen, K.C., Sapinoro, R.E., Kottmann, R.M., Kulkarni, A.A., Iismaa, S.E., Johnson, G.V., Thatcher, T.H., Phipps, R.P., and Sime, P.J. (2011). Transglutaminase 2 and its role in pulmonary fibrosis. Am J Respir Crit Care Med *184*, 699-707.

Parikh, V.N., Jin, R.C., Rabello, S., Gulbahce, N., White, K., Hale, A., Cottrill, K.A., Shaik, R.S., Waxman, A.B., Zhang, Y.Y.*, et al.* (2012). MicroRNA-21 Integrates Pathogenic Signaling to Control Pulmonary Hypertension: Results of a Network Bioinformatics Approach. Circulation *125*, 1520-1532.

Preaux, A.M., Mallat, A., Nhieu, J.T., D'Ortho, M.P., Hembry, R.M., and Mavier, P. (1999). Matrix metalloproteinase-2 activation in human hepatic fibrosis regulation by cell-matrix interactions. Hepatology *30*, 944-950.

Prele, C.M., Yao, E., O'Donoghue, R.J., Mutsaers, S.E., and Knight, D.A. (2012). STAT3: a central mediator of pulmonary fibrosis? Proc Am Thorac Soc *9*, 177-182.

Putman, R.K., Rosas, I.O., and Hunninghake, G.M. (2014). Genetics and early detection in idiopathic pulmonary fibrosis. Am J Respir Crit Care Med *189*, 770-778.

Reddy, V., Meyrick, B., Wong, J., Khoor, A., Liddicoat, J., Hanley, F., and Fineman, J. (1995). In utero placement of aortopulmonary shunts. A model of postnatal pulmonary hypertension with increased pulmonary blood flow in lambs. Circulation *92*, 606-613.

Reichenbach, V., Ros, J., Fernandez-Varo, G., Casals, G., Melgar-Lesmes, P., Campos, T., Makriyannis, A., Morales-Ruiz, M., and Jimenez, W. (2012). Prevention of fibrosis progression in CCl4-treated rats: role of the hepatic endocannabinoid and apelin systems. J Pharmacol Exp Ther *340*, 629-637.

Ren, S., Johnson, B.G., Kida, Y., Ip, C., Davidson, K.C., Lin, S.L., Kobayashi, A., Lang, R.A., Hadjantonakis, A.K., Moon, R.T.*, et al.* (2013). LRP-6 is a coreceptor for multiple fibrogenic signaling pathways in pericytes and myofibroblasts that are inhibited by DKK-1. Proc Natl Acad Sci U S A *110*, 1440-1445.

Safaeian, L., Abed, A., and Vaseghi, G. (2014). The role of Bcl-2 family proteins in pulmonary fibrosis. Eur J Pharmacol *741*, 281-289.

Selman, M., Ruiz, V., Cabrera, S., Segura, L., Ramirez, R., Barrios, R., and Pardo, A. (2000). TIMP-1, -2, -3, and -4 in idiopathic pulmonary fibrosis. A prevailing nondegradative lung microenvironment? Am J Physiol Lung Cell Mol Physiol *279*, L562-574.

Sfikakis, P.P. (2011). Is IL-4 a potential therapeutic target in systemic sclerosis-associated pulmonary fibrosis? Clin Immunol *141*, 240-241.

Shi, W., Bellusci, S., and Warburton, D. (2007). Lung development and adult lung diseases. Chest *132*, 651-656.

Sime, P.J. (2008). The antifibrogenic potential of PPARgamma ligands in pulmonary fibrosis. J Investig Med *56*, 534-538.

Smyth, G.K., Michaud, J., and Scott, H.S. (2005). Use of within-array replicate spots for assessing differential expression in microarray experiments. Bioinformatics *21*, 2067-2075.

Sokolovic, A., Rodriguez-Ortigosa, C.M., Bloemendaal, L.T., Oude Elferink, R.P., Prieto, J., and Bosma, P.J. (2013). Insulin-like growth factor 1 enhances bile-duct proliferation and fibrosis in Abcb4(-/-) mice. Biochim Biophys Acta *1832*, 697-704.

Steiner, M.K., Syrkina, O.L., Kolliputi, N., Mark, E.J., Hales, C.A., and Waxman, A.B. (2009). Interleukin-6 overexpression induces pulmonary hypertension. Circ Res *104*, 236-244, 228p following 244.

Sweetwyne, M.T., and Murphy-Ullrich, J.E. (2012). Thrombospondin1 in tissue repair and fibrosis: TGF-beta-dependent and independent mechanisms. Matrix Biol *31*, 178-186.

Swigris, J.J., and Brown, K.K. (2010). The role of endothelin-1 in the pathogenesis of idiopathic pulmonary fibrosis. BioDrugs *24*, 49-54.

Trombetta-Esilva, J., and Bradshaw, A.D. (2012). The Function of SPARC as a Mediator of Fibrosis. Open Rheumatol J *6*, 146-155.

Tsutsumi, H., Tanaka, T., Ohashi, N., Masuno, H., Tamamura, H., Hiramatsu, K., Araki, T., Ueda, S., Oishi, S., and Fujii, N. (2007). Therapeutic potential of the chemokine receptor CXCR4 antagonists as multifunctional agents. Biopolymers *88*, 279-289.

Uchinami, H., Seki, E., Brenner, D.A., and D'Armiento, J. (2006). Loss of MMP 13 attenuates murine hepatic injury and fibrosis during cholestasis. Hepatology *44*, 420-429.

van Dongen, S., Abreu-Goodger, C., and Enright, A.J. (2008). Detecting microRNA binding and siRNA off-target effects from expression data. Nat Methods *5*, 1023-1025.

Vetrone, S.A., Montecino-Rodriguez, E., Kudryashova, E., Kramerova, I., Hoffman, E.P., Liu, S.D., Miceli, M.C., and Spencer, M.J. (2009). Osteopontin promotes fibrosis in dystrophic mouse muscle by modulating immune cell subsets and intramuscular TGF-beta. J Clin Invest *119*, 1583-1594.

Vuga, L.J., Ben-Yehudah, A., Kovkarova-Naumovski, E., Oriss, T., Gibson, K.F., Feghali-Bostwick, C., and Kaminski, N. (2009). WNT5A is a regulator of fibroblast proliferation and resistance to apoptosis. Am J Respir Cell Mol Biol *41*, 583-589.

Wynes, M.W., Edelman, B.L., Kostyk, A.G., Edwards, M.G., Coldren, C., Groshong, S.D., Cosgrove, G.P., Redente, E.F., Bamberg, A., Brown, K.K.*, et al.* (2011). Increased cell surface Fas expression is necessary and sufficient to sensitize lung fibroblasts to Fas ligation-induced apoptosis: implications for fibroblast accumulation in idiopathic pulmonary fibrosis. J Immunol *187*, 527-537.

Wynn, T.A., and Ramalingam, T.R. (2012). Mechanisms of fibrosis: therapeutic translation for fibrotic disease. Nat Med *18*, 1028-1040.

Yamashita, C.M., Dolgonos, L., Zemans, R.L., Young, S.K., Robertson, J., Briones, N., Suzuki, T., Campbell, M.N., Gauldie, J., Radisky, D.C.*, et al.* (2011). Matrix metalloproteinase 3 is a mediator of pulmonary fibrosis. Am J Pathol *179*, 1733-1745.

Yang, J.J., Tao, H., Huang, C., and Li, J. (2013). Nuclear erythroid 2-related factor 2: a novel potential therapeutic target for liver fibrosis. Food Chem Toxicol *59*, 421-427.

Yoshida, T., Ogata, H., Kamio, M., Joo, A., Shiraishi, H., Tokunaga, Y., Sata, M., Nagai, H., and Yoshimura, A. (2004). SOCS1 is a suppressor of liver fibrosis and hepatitis-induced carcinogenesis. J Exp Med *199*, 1701-1707.

Yukawa, K., Kishino, M., Goda, M., Liang, X.M., Kimura, A., Tanaka, T., Bai, T., Owada-Makabe, K., Tsubota, Y., Ueyama, T.*, et al.* (2005). STAT6 deficiency inhibits tubulointerstitial fibrosis in obstructive nephropathy. Int J Mol Med *15*, 225-230.

Zardi, E.M., Navarini, L., Sambataro, G., Piccinni, P., Sambataro, F.M., Spina, C., and Dobrina, A. (2013). Hepatic PPARs: their role in liver physiology, fibrosis and treatment. Curr Med Chem *20*, 3370-3396.

Zhang, G., Kernan, K.A., Collins, S.J., Cai, X., Lopez-Guisa, J.M., Degen, J.L., Shvil, Y., and Eddy, A.A. (2007). Plasmin(ogen) promotes renal interstitial fibrosis by promoting epithelial-to-mesenchymal transition: role of plasmin-activated signals. J Am Soc Nephrol *18*, 846-859.

Zhang, Y.M., Bo, J., Taffet, G.E., Chang, J., Shi, J., Reddy, A.K., Michael, L.H., Schneider, M.D., Entman, M.L., Schwartz, R.J.*, et al.* (2006). Targeted deletion of ROCK1 protects the heart against pressure overload by inhibiting reactive fibrosis. FASEB J *20*, 916-925.

Zhou, H., Li, Y.J., Wang, M., Zhang, L.H., Guo, B.Y., Zhao, Z.S., Meng, F.L., Deng, Y.G., and Wang, R.Y. (2011). Involvement of RhoA/ROCK in myocardial fibrosis in a rat model of type 2 diabetes. Acta Pharmacol Sin *32*, 999-1008.

Zhou, X., Hovell, C.J., Pawley, S., Hutchings, M.I., Arthur, M.J., Iredale, J.P., and Benyon, R.C. (2004). Expression of matrix metalloproteinase-2 and -14 persists during early resolution of experimental liver fibrosis and might contribute to fibrolysis. Liver Int *24*, 492-501.